Next Materials 8 (2025) 100695

Contents lists available at ScienceDirect

Next Materials

journal homepage: www.sciencedirect.com/journal/next-materials

Research article

Structural and magnetic properties of hydrothermally synthesized Ca-doped hematite

A.Y. Mironovich [a], G.A. Skorlupin [a,*], V.G. Kostishin [a], A.I. Ril [b], R.I. Shakirzyanov [c], E.S. Savchenko [a]

[a] National University of Science and Technology "MISIS", Leninsky Prospect, 4, Moscow 119049, Russia
[b] Kurnakov Institute of General and Inorganic Chemistry, Russian Academy of Sciences (IGIC RAS), Leninsky Prospekt, 31, Moscow 119991, Russia
[c] Engineering Profile Laboratory, L.N. Gumilyov Eurasian National University, Nur-Sultan 010008, Kazakhstan

ARTICLE INFO

Keywords:
Magnetic Materials
Hematite
Mössbauer Spectroscopy
Magnetic Properties
X-Ray Diffraction

ABSTRACT

Powders of calcium-substituted hematite were synthesized via hydrothermal method. The samples were characterized using X-ray diffraction, Mössbauer spectroscopy, scanning electron microscopy, energy-dispersive X-ray spectroscopy, Fourier-transform infrared spectroscopy, and magnetometry. Structural analysis revealed that Ca-substituted samples maintained single-phase hematite for Fe/Ca ratios between 11 and 5. Further increase in calcium concentration led to formation of a defective iron-calcium spinel phase. Infrared spectra confirmed the presence of hydroxyl groups within the hematite lattice. The incorporation of calcium and associated defects significantly influenced the magnetic properties of hematite, inducing ferromagnetic behavior. The maximum magnetization value of 12.9 emu/g was achieved at Fe/Ca = 6, representing a substantial enhancement compared to most other doped hematites. These materials show potential for applications in hyperthermia, MRI contrast enhancement, and wastewater treatment.

1. Introduction

Hematite, or α-Fe_2O_3, is a well-studied compound that is valued for its electrical and magnetic properties, non-toxicity, chemical stability and abundance. Because of its properties, hematite has been successfully used in catalysis [1], medicine [2], sensing [3] and ecology [4]. The magnetic properties are critical in hyperthermic treatment, MRI contrast and drug delivery applications. Strong magnetism is also useful for particle recovery after wastewater treatment. Undoped α-Fe_2O_3 exhibits antiferromagnetic or weak ferromagnetic behavior due to the nearly antiparallel orientation of the Fe^{3+} spins in adjacent (111) planes [5]. To enhance the magnetic properties of this material a wide variety of cations have been used as substituents in the hematite structure [6–8]. However, studies of substituted hematite do not always provide data of magnetic measurements due to the specifics of the subject, for example investigation of gas-sensitive [9–12] or catalytic [13,14] properties. Still, there are many studies that demonstrate no significant changes in the magnetic parameters of hematite after addition of different elements to its lattice: Ga^{3+} [15], Eu^{3+} [16], Mn^{2+} [7], Sn^{4+} [17], Ce^{3+} [18], Er^{3+} [19], Zn^{2+} [20], Ru^{3+} [21], Ca^{2+} [22]. Other works have shown that the substitution of Gd^{3+} [23], Cu^{2+} [7] or Co^{2+} [7] can provide hematite with outstanding magnetic parameters.

In this work we have synthesized Ca-substituted hematite via hydrothermal method. Calcium was chosen as the doping element because it is widely distributed in nature, cheap, environmentally friendly and biocompatible. The focus of the study is on the magnetic and structural properties, the improvement of which with a widely available dopant is important for applications such as hyperthermia, MRI contrast, and particle extraction by a magnetic field after wastewater treatment.

2. Experimental

Powders of substituted α-Fe_2O_3 were prepared by hydrothermal synthesis. The precursor was a mixture of an aqueous solution of iron nitrate nonahydrate $Fe(NO_3)_3 \bullet 9H_2O$ and calcium nitrate $Ca(NO_3)_2$ with an aqueous solution of sodium hydroxide NaOH in proportion 60 ml/20 ml, respectively. The solutions were prepared so that the concentrations of ferric and hydroxide ions in the total volume (80 ml) were 0.25 M and 2 M respectively. The amount of calcium nitrate was added in order to obtain Fe^{3+}/Ca^{2+} molar ratios of 11, 9, 7, 6, 5, 4 and 3.

* Corresponding author.
E-mail address: skorlupin.ga@misis.ru (G.A. Skorlupin).

https://doi.org/10.1016/j.nxmate.2025.100695
Received 21 February 2025; Received in revised form 19 April 2025; Accepted 2 May 2025
Available online 13 May 2025

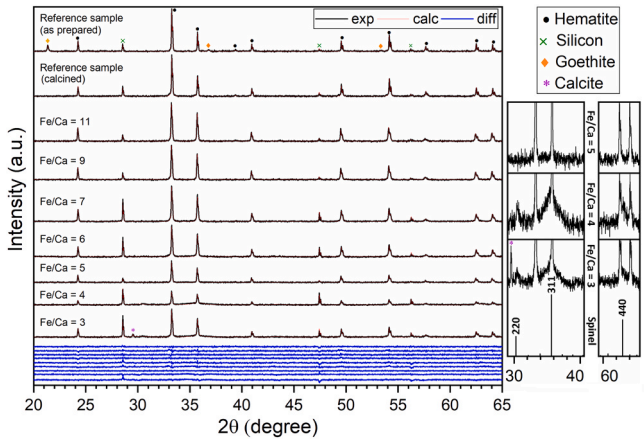

Fig. 1. XRD patterns of the samples obtained.

The prepared solutions were mixed in a 100 ml Teflon vessel, sealed, and placed in an oven. The autoclave was slowly heated to 180 °C for 2 h and kept at this temperature for 4 h. Separation of the precipitate formed and the liquid solution was carried out by decantation, followed by washing of the precipitate with distilled water until pH 7 was reached. The precipitate was then dried at 90 °C for 8 h. The dry residue was ground in a mortar. A reference sample without calcium addition was also prepared under the same conditions. According to the results obtained, this sample was additionally calcined at 330 °C for 1 h in an air atmosphere.

The study of the phase composition of the powder was carried out using Mössbauer spectroscopy (MS) on the EM MS-1104 apparatus with Co^{57} in rhodium matrix as γ-source. The isomeric shift was calculated relative to α-Fe. X-ray diffraction (XRD) studies were performed at the Center of Shared Equipment of IGIC RAS using a Bruker D8 Advance X-ray diffractometer (CuKα radiation, λ= 0.154 nm, U= 40 kV, I= 40 mA). Prior to measurement, a ground silicon crystal was added to the samples as a reference for the calculation of lattice parameters. Fourier-transform infrared spectroscopy (FTIR) data were recorded on an FTIR InfraLUM FT-08 spectrometer. Measurements were made in the range of 400–4000 cm^{-1}. Spectra were recorded in 20 scans with a resolution of 2 cm^{-1} using an ATR (Pike) attachment at room temperature. The magnetic parameters of the samples were measured using JDAW-2000D vibrating-sample magnetometer (VSM). The morphology and general view of the obtained powders were analyzed by scanning electron microscopy (SEM) method on the Hitachi TM3030 (Japan) microscope with the 15 kV acceleration voltage. To avoid charging of insulating powders 20 nm of Au was deposited by magnetron sputtering in the CCU-010 coating machine. Energy Dispersive X-ray spectroscopy (EDX) for elemental mapping and chemical composition evaluation was performed on the Bruker Quantax 75 system.

3. Results and discussion

Fig. 1 displays the XRD patterns of the synthesized samples, with refined parameters summarized in Table 1. Single-phase hematite (α-Fe_2O_3) was confirmed for samples with Fe/Ca ratios between 11 and 5. For Fe/Ca = 4 and 3, the broad halo centered at the (110) hematite peak (35.7°) indicates potential secondary phase formation or significant structural disorder (Fig. 1, right panel). The XRD patterns of these samples also show low-intensity broad peaks at 30.5° and 63.2°. Together with the halo at 35.7°, these peaks may correspond to a spinel phase. Spinels have cubic structure ($Fd\bar{3}m$, No. 227) with general formula $Me^{2+}Me^{3+}_2O_4$ (Me^{2+} = Zn, Mg, Fe; Me^{3+} = Al, Fe, Cr). Although $CaFe_2O_4$ follows the same stoichiometry, it typically crystallizes in an orthorhombic structure (*Pnma*, No. 62) due to the large ionic radius of Ca^{2+}. However, certain synthesis routes have yielded metastable cubic $CaFe_2O_4$ as reported elsewhere [24–26]. Thus, we suggest the formation of a non-stoichiometric iron-calcium spinel phase. The significant peak broadening implies high defect concentration, chemical inhomogeneity, or nanocrystallinity, potentially causing calcium deficiency that stabilizes the spinel structure. For Rietveld refinement, the spinel phase was fitted with the maghemite (γ-Fe_2O_3) reference, as its lattice parameter matches the observed phase (a = 8.34 Å). In addition, the Fe/Ca = 3 diffraction pattern shows a calcite ($CaCO_3$) peak. Apparently, this phase arises from reaction of excess calcium with CO_2 (either atmospheric or dissolved in water).

The reference sample contained goethite (α-FeOOH) as a secondary phase – a common byproduct of iron oxide hydrothermal synthesis. Notably, Ca^{2+} addition completely suppresses goethite formation, producing single-phase hematite for Fe/Ca ratios ≥ 5. In [27] it was shown that acicular goethite particles are preferentially formed at high concentrations of OH^- anions. In the reference sample, the chosen conditions provided such an excess of hydroxyl groups. Next, apparently, the addition of Ca^{2+} ions to the solution reduces the concentration of free OH^- by binding them into insoluble $Ca(OH)_2$. Moreover, [27] demonstrates that hematite particle morphology depends critically on OH^- amount: rhombohedral crystals are favored at low OH^- concentration, while disk-shaped particles form at high OH^- concentration. In our work, we observe the identical morphological transition from disks to rhombohedra (Fig. 2), suggesting that Ca^{2+} addition reduces free OH^- concentration. However, in samples with Fe/Ca ≤ 7, small plate-like or flake particles appear alongside rhombohedral crystals. This demonstrates that particle morphology depends not exclusively on free OH^- concentration but is also determined by Ca^{2+} ions.

As Ca^{2+} and Fe3+ exhibit significant differences in charge and ionic radii [28], calcium incorporation into the hematite lattice requires verification. The EDX spectra (Fig. 3) and elemental mapping (Fig. 4) confirm calcium presence in the synthesized powders.

The XRD structural data reveal that the lattice parameters and volume of the Fe/Ca = 11 sample are larger than those of the reference sample, confirming calcium incorporation (Table 1, Fig. 5). However, with further Ca^{2+} addition, both lattice parameters and unit cell volume decrease, despite Ca^{2+} being larger than Fe^{3+} . This lattice contraction suggests that the system compensates for the size mismatch through other structural changes. We propose three lattice reduction mechanisms associated with charge compensation: partial oxidation of Fe^{3+} to Fe^{4+}, oxygen vacancy generation, and OH^- substitution for O^{2-} balanced by Fe^{3+} vacancies.

Table 1
Rietveld refined parameters of obtained hematite samples.

Fe/Ca Ratio	Reference sample	11	9	7	6	5	4	3
R_{wp}, %	1.21	1.09	1.13	1.4	1.46	1.49	1.55	1.49
R_{exp}, %	1.14	1.03	1.06	1.21	1.21	1.41	1.32	1.22
χ^2	1.13	1.12	1.14	1.34	1.46	1.12	1.38	1.49
a, Å	5.0356	5.0408	5.0408	5.0404	5.0404	5.0400	5.0399	5.0397
c, Å	13.7582	13.7743	13.7713	13.7693	13.7687	13.7659	13.7682	13.7659

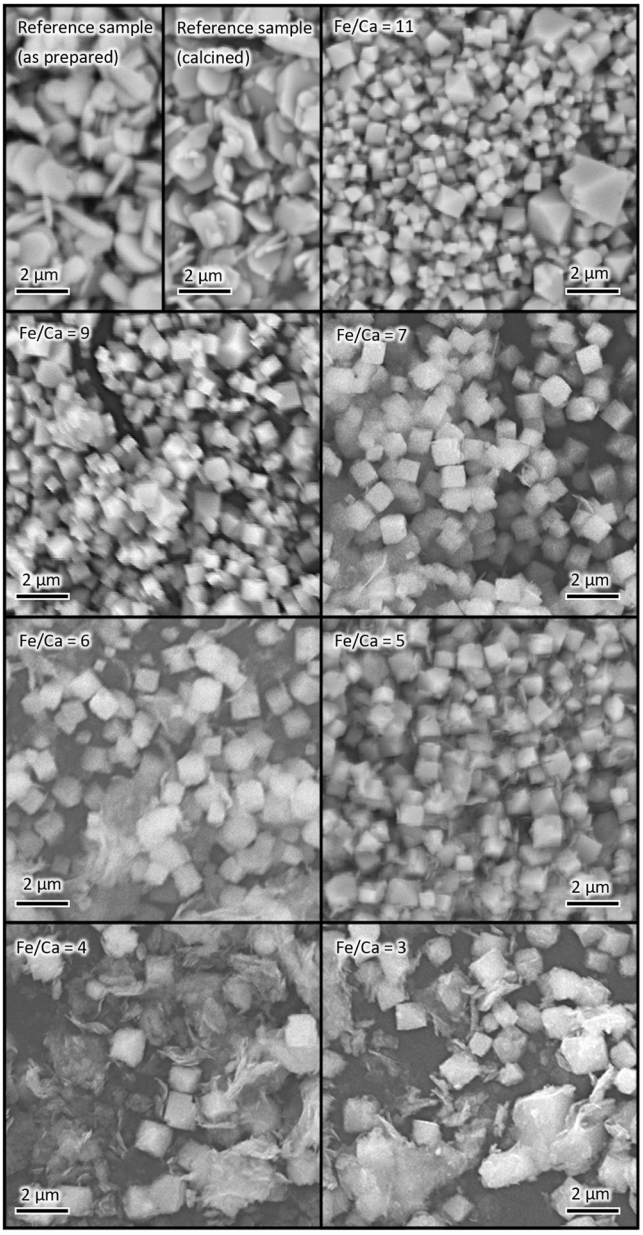

Fig. 2. SEM images of hydrothermally synthesized hematite.

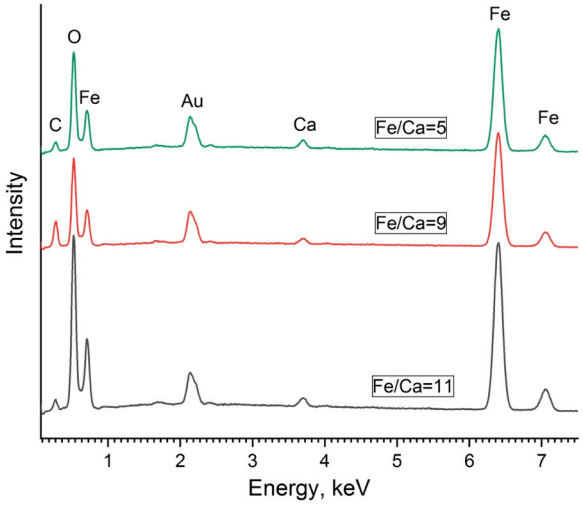

Fig. 3. EDX spectra of Ca-doped hematite.

The ionic radius of Fe^{4+} is smaller than Fe^{3+} [28], enabling lattice contraction through this valence change. Substantial evidence supports this charge compensation mechanism [29–32], including confirmation of Fe^{4+} formation under hydrothermal conditions [33]. To determine the iron oxidation state in our samples, we used Mössbauer spectroscopy as one of the most suitable techniques for this task.

The Mössbauer spectra and corresponding parameters (Fig. 6, Table 2) show no evidence of Fe^{4+} ions. The reference sample's spectrum was fitted with three sextets: one corresponding to goethite and two to hematite (Table 2). Typically, hematite's Mössbauer spectrum is fitted with a single sextet [34]. However, hematite with small particle sizes or structural defects may show additional sextets with reduced hyperfine fields [35–37]. Taking into account the particle sizes (Fig. 2), the second sextet appears to represent the defect fraction of the phase rather than the surface contribution. The Ca-substituted hematite samples (Fe/Ca = 11 and 9) were fitted with the same two hematite sextets: one for bulk hematite (standard) and another for defective fraction. Notably, while the spectra of Fe/Ca = 11 and 9 samples show no significant differences, the Fe/Ca = 7 and 6 samples required an additional sextet for adequate fitting. This new component, designated as NEP-1 (Non-Equivalent Position), corresponds to a Fe^{3+} in hematite lattice with substantially reduced hyperfine field (H_{eff}). At even higher calcium concentrations (Fe/Ca = 5), a distinct new sextet (NEP-2) appears in the Mössbauer spectrum. Unlike NEP-1, this component shows an increased hyperfine field (H_{eff} = 536 kOe) compared to standard hematite, suggesting different local environments around the iron nuclei.

The final two spectra (Fe/Ca = 4 and 3) differ dramatically from the others, requiring seven sextets for fitting. Two of these sextets match the standard and defective hematite components observed in previous samples. Two additional sextets with isomer shift values of 0.28 and 0.19 mm/s clearly indicate Fe^{3+} in tetrahedral coordination. This finding agrees with XRD data confirming the presence of a spinel phase in these samples. The remaining four sextets correspond Fe^{3+} in octahedral coordination, though we cannot reliably distinguish whether they originate from the spinel phase or NEP in hematite. The most significant variation between these sextets lies in their hyperfine field values.

The reduction in hyperfine fields may result from disrupted Fe-O-Fe superexchange interactions, potentially caused by three factors: cation substitution (Fe^{3+} replaced by Ca^{2+}; Fe-O-Ca), anion vacancies (missing oxygen; Fe-□-Fe) and cation vacancies (missing iron; Fe-O-□). These structural modifications alter the local magnetic environment, leading to the formation of new iron sites with distinct hyperfine field values. Among these possible mechanisms, cation substitution aligns most directly with our experimental design. However, oxygen vacancy formation offers critical advantages – it simultaneously explains both the observed lattice contraction and charge compensation (requiring one vacancy per two Ca^{2+} ions). This mechanism has been experimentally confirmed in similar systems [13], supporting its relevance to our study. Also, the observed lattice volume reduction with increasing calcium

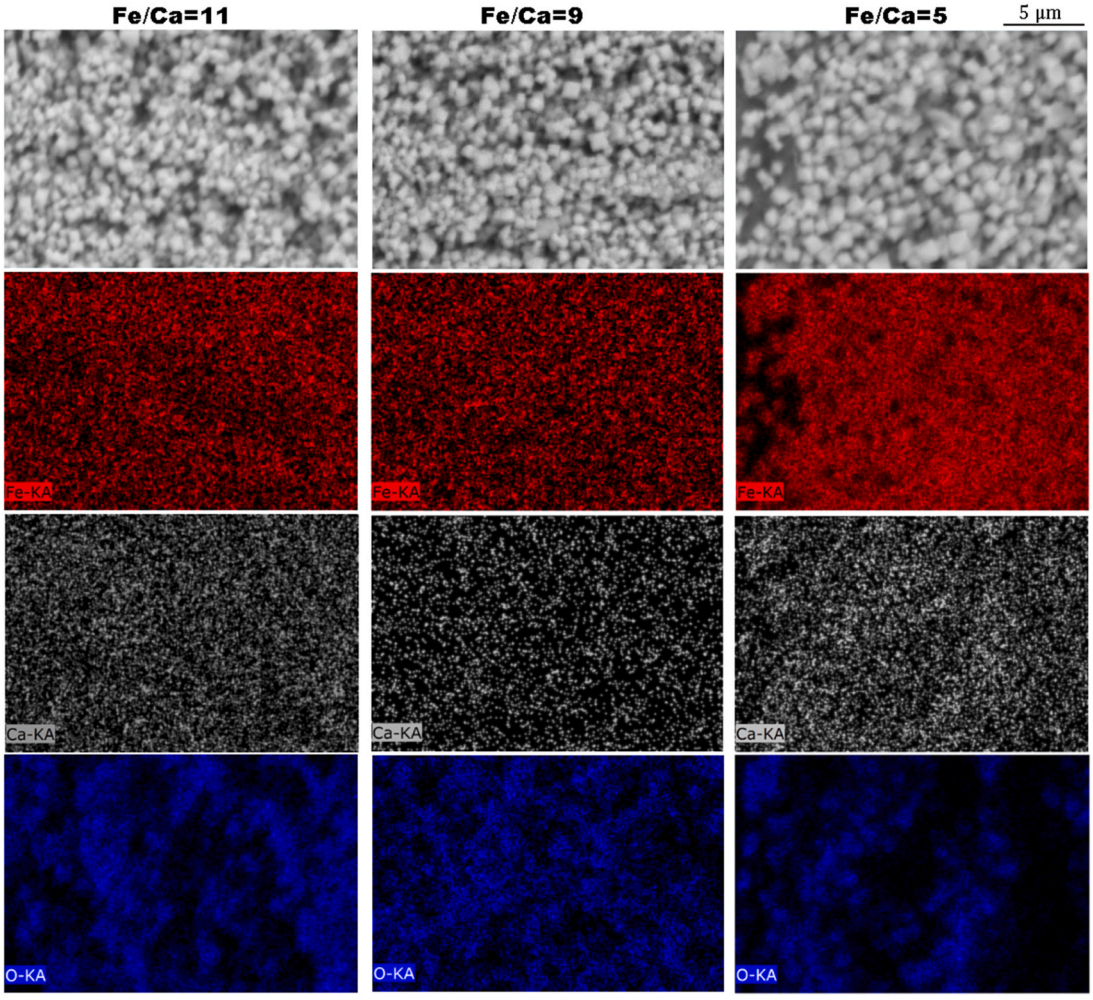

Fig. 4. EDX elemental mapping analysis of Ca-doped hematite.

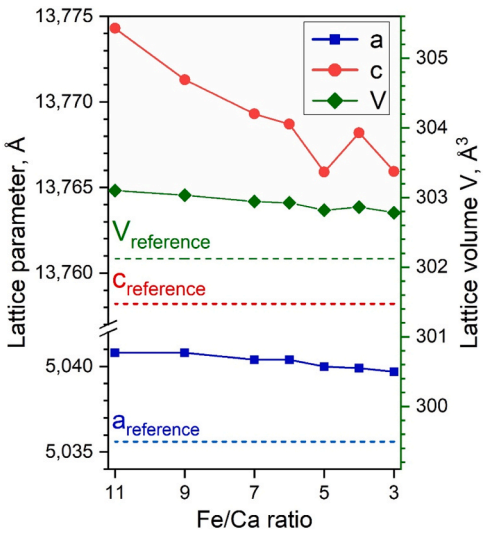

Fig. 5. Dependencies of hematite lattice parameters on Fe/Ca ratio.

content can be explained by rising oxygen vacancy concentrations, as was suggested above.

In addition, partial substitution of O^{2-} with OH^- is also possible. Hematite-like materials containing structural OH^- groups are known as hydrohematites [38]. According to different studies, replacement of O^{2-} with OH^- in hematite affects lattice parameters in complex ways [39,40], eventually reducing lattice volume. This contraction may be related to Fe^{3+} vacancy formation required for electrostatic neutrality. The chemical formula of such a compound is $Fe_{(2-x/3)}(OH)_xO_{3-x}$ and it could be changed to $Fe_{(2-y-x/3)}Ca_y(OH)_xO_{3-x}$ in case of Ca-substituted hydrohematites. Therefore, hydroxyl incorporation may produce effects similar to oxygen vacancies, including lattice contraction and additional sextets in Mössbauer spectra.

FTIR spectroscopy is one of the best methods to confirm the presence of hydrogen in hematite lattice. Hydrohematite FTIR spectra has a broad peak at 900–950 cm^{-1}, which is related to O-H vibrations and absent in stoichiometric α-Fe_2O_3 [38,41].

FTIR spectra of the samples obtained are presented at Fig. 7. In addition to main band of hematite (516 and 427 cm^{-1}) the spectrum of reference sample has peaks at 798, 900 and 3110 cm^{-1} which can be attributed to goethite. After calcination goethite peaks disappeared, revealing a broad complex band near 900 cm^{-1} which is a feature of hydrohematite. This band present in all samples, confirming that some O^{2-} ions were replaced for OH^-. Besides, these samples also had a small peak at 790 cm^{-1} which was not observed in hydrohematites spectra [41]. However, as it close to goethite 798 cm^{-1} band, it is also should be attributed to O-H vibrations. These data confirm the presence of hydrogen in the hematite lattice. Moreover, the spectrum of sample with Fe/Ca= 5 ratio has an additional peak at 750 cm^{-1}. According to IR spectra of different iron oxides and oxyhydroxides this peak may be attributed to O-H vibrations in lepidocrocite (γ-FeOOH) [42,43].

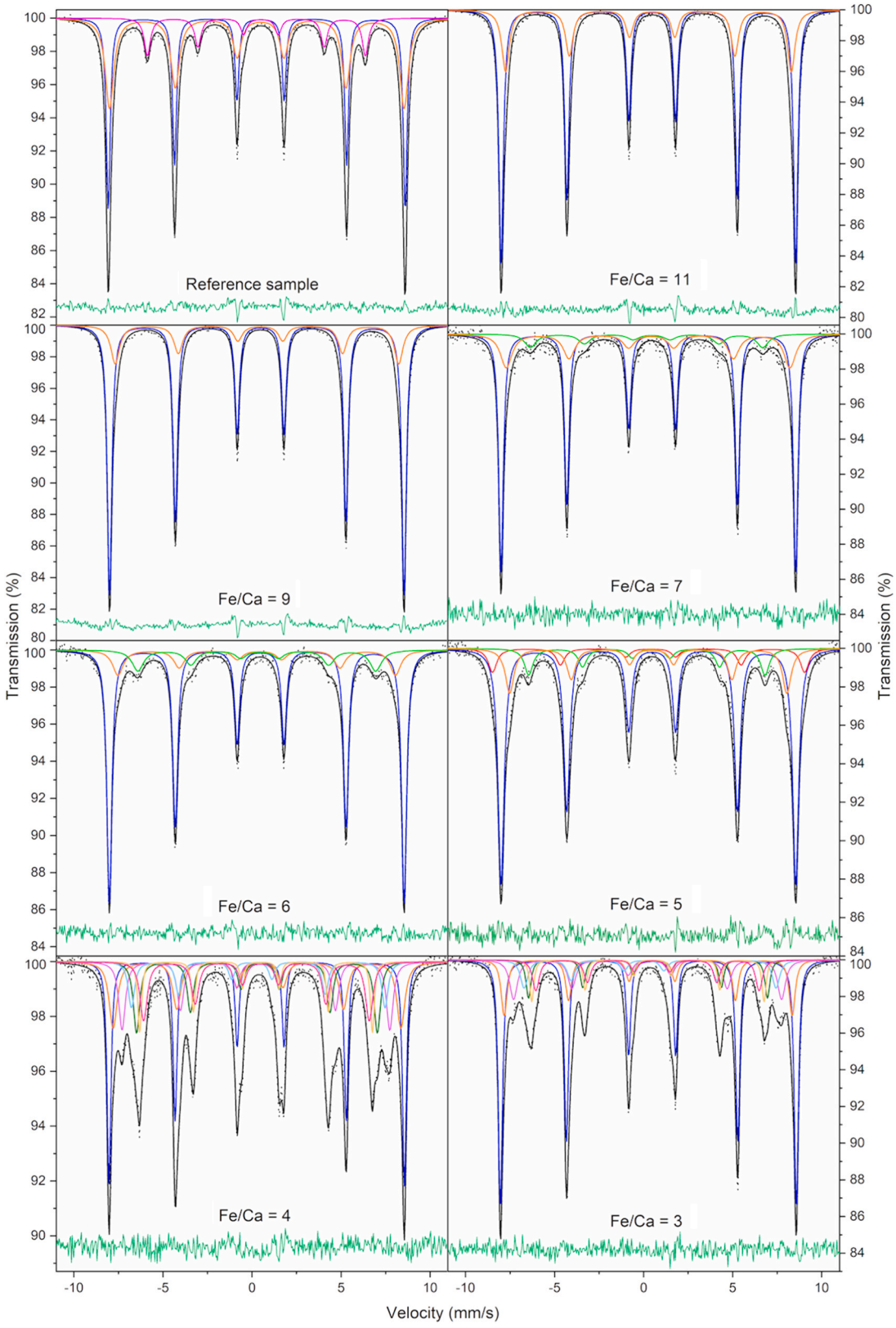

Fig. 6. Mössbauer spectra of the samples.

Table 2
Mössbauer data of the samples.

Fe/Ca ratio	Component	IS, mm/s	QS, mm/s	H_{eff}, kOe	S, %	Γ, mm/s
Reference sample	Standard	0.37	−0.22	518	43.13	0.27
	Defective	0.37	−0.21	514	43.77	0.58
	Goethite	0.37	−0.27	380	13.10	0.42
11	Standard	0.37	−0.21	514	68.58	0.29
	Defective	0.37	−0.21	498	31.42	0.50
9	Standard	0.37	−0.21	513	67.79	0.28
	Defective	0.37	−0.21	500	32.21	0.58
7	Standard	0.37	−0.21	514	67.1	0.30
	Defective	0.34	−0.18	495	23.49	0.78
	NEP−1	0.31	−0.28	405	9.41	0.78
6	Standard	0.37	−0.22	514	69.66	0.33
	Defective	0.35	−0.17	486	17.15	0.77
	NEP−1	0.35	−0.17	415	13.19	0.77
5	Standard	0.37	−0.21	514	45.95	0.34
	Defective	0.36	−0.19	491	28.7	0.78
	NEP−1	0.31	−0.22	411	10.09	0.71
	NEP−2	0.37	−0.18	536	15.26	0.78
4	Standard	0.37	−0.22	515	26.22	0.26
	Defective	0.37	−0.17	502	16.2	0.55
	Tetrahedral−1	0.28	−0.11	467	13.78	0.45
	Tetrahedral−2	0.17	0.36	442	8.79	0.42
	Octahedral−1	0.37	−0.18	420	13.55	0.42
	Octahedral−2	0.36	−0.27	406	8.58	0.26
	Octahedral−3	0.36	−0.23	393	12.89	0.51
3	Standard	0.37	−0.21	516	42.09	0.28
	Defective	0.36	−0.21	502	13.22	0.40
	Tetrahedral−1	0.28	−0.11	468	12.8	0.53
	Tetrahedral−2	0.19	0.34	439	8.49	0.5
	Octahedral−1	0.36	−0.23	416	7.83	0.33
	Octahedral−2	0.37	−0.25	405	6.86	0.27
	Octahedral−3	0.35	−0.26	389	8.7	0.45

IS, QS, H_{eff}, Γ and S are isomer shift, quadrupole splitting, effective magnetic field on Fe^{57} nuclei, line width and relative contribution of subspectrum, respectively.

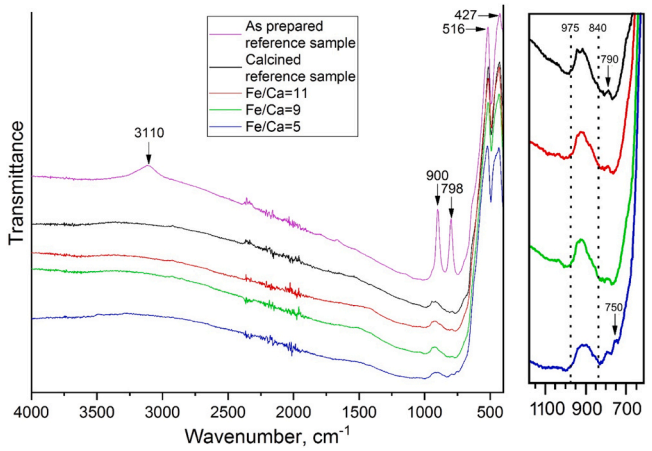

Fig. 7. IR spectra of reference sample and Ca-doped hematite samples.

However, there are no other bands of lepidocroicite. Also, the component corresponding to this phase [44] was not observed on Mössbauer spectra. Thus, we assume that peak at 750 cm^{-1} represent O-H vibrations in hematite lattice. Apparently, the sample with Fe/Ca = 5 contains more hydrogen in comparison with other samples, which result in some structural transformations and appearance of additional vibration modes.

The structural features of hydrothermally synthesized calcium-substituted hematite can be summarized as follows. Hydrogen incorporation occurs regardless of Ca presence, as confirmed by FTIR spectroscopy. The larger ionic radius of Ca^{2+} compared to Fe^{3+} would suggest lattice expansion, yet increasing calcium concentration results in lattice contraction instead. This phenomenon can be attributed to two concurrent charge compensation mechanisms: oxygen vacancy formation and partial substitution of O^{2-} with OH^{-} accompanied by Fe^{3+} vacancy generation. The presence of calcium ions, oxygen vacancies, hydroxyl groups, and iron vacancies generates a different local environment for iron cations within the hematite structure. The resulting non-equivalent sites are identified through Mössbauer spectroscopy. Apparently, the component «defective» related to hydrogen incorporation, as it can be found in all spectra regardless of calcium presence. In opposite, the components NEP-1 and NEP-2 corresponds to Fe having Ca in local environment, as these sextets appeared in Ca-rich samples.

The magnetic hysteresis loops of the samples are shown in Fig. 8. The calcium-free sample was two-phase, which makes comparison with other samples slightly incorrect. To get rid of goethite, the sample was calcined at 330 °C, which is enough according to literature [45] and effective, as can be observed with XRD and FTIR. A small addition of calcium (Fe/Ca = 11) slightly decreases the magnetization to 1 emu/g. However, a further increase in the calcium concentration led to some increase in the magnetic properties. First, this increase was insufficient (3 emu/g for Fe/Ca = 9). Next, the magnetization becomes noticeable (from 7.8 emu/g to 12.9 emu/g for Fe/Ca = 7, 6, 5). This effect may be due to defects in hematite lattice, which modify magnetic ordering and enhance natural weak ferromagnetism of α-Fe_2O_3. Also changes in magnetic behavior correlate with formation of additional sextets on Mössbauer spectra of these samples. The presence of several sextets with different H_{eff} values is a sign of ferrimagnetic ordering, which could explain an increase in magnetization. Saturation state also could be interpreted as formation of ferrimagnetic structure. Nevertheless, the measured values of saturation magnetization are much higher than that of most other samples of substituted hematites [15–22]. The combination of low coercivity and enhanced magnetization enables the synthesized powders to interact effectively with permanent magnets. This property makes them suitable for practical applications requiring magnetic separation, such as water treatment processes and other technologies utilizing extractable magnetic particles.

The samples with Fe/Ca = 4 and 3 exhibit significant magnetization values of 40.5 emu/g and 29.6 emu/g, respectively. This enhancement results from spinel phase formation, as confirmed by XRD and MS. The sample with Fe/Ca = 4 shows stronger magnetic properties due to its higher spinel content. As was demonstrated with XRD, at higher calcium content (Fe/Ca = 3), a separate non-magnetic calcite phase forms. This may reduce calcium availability for incorporation into the hematite lattice, restricting spinel phase formation.

4. Conclusions

A series of Ca-doped Fe_2O_3 fine powders was successfully prepared by hydrothermal synthesis with various Fe^{3+}/Ca^{2+} ratios in the initial solution. The presence of calcium in the reaction system fundamentally altered the crystallization process, suppressing goethite formation and promoting rhombohedral hematite morphology over plate-like crystals. Single-phase hematite was obtained for Fe/Ca ratios between 11 and 5, while higher calcium concentrations (Fe/Ca ≤ 4) led to the formation of a defective iron-calcium spinel side phase. The partial substitution of Fe^{3+} with Ca^{2+} ions in the hematite lattice appears to be accompanied by oxygen vacancy formation, partial replacement of O^{2-} by OH^{-}, and generation of Fe^{3+} vacancies. These defects induce significant local structural distortions, ultimately modifying the magnetic properties of the samples and resulting in ferri/ferromagnetic behavior. Of particular

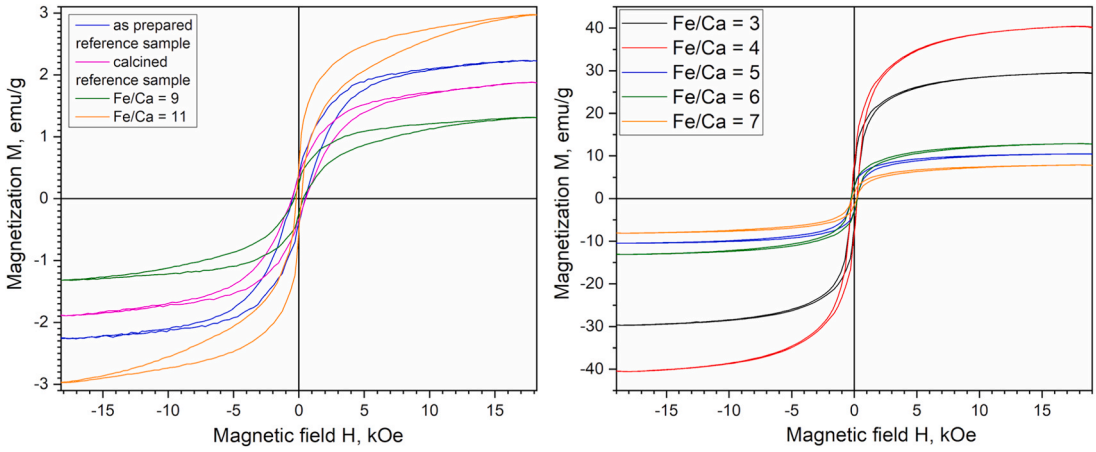

Fig. 8. Room temperature hysteresis loops of hydrothermally synthesized hematite samples.

interest, samples with intermediate calcium content (Fe/Ca = 7, 6, 5) demonstrated remarkable saturation magnetization (7.8–12.9 emu/g), representing a significant enhancement over pure hematite.

Declaration of Competing Interest

The authors declare that they have no known competing financial interests or personal relationships that could have appeared to influence the work reported in this paper

Acknowledgments

The study was supported by Russian Science Foundation, grant N° 24–13–00268 (NUST MISIS topic N°8219305).

References

[1] J. Li, J. You, Z. Wang, Y. Zhao, J. Xu, X. Li, H. Zhang, Application of α-Fe_2O_3-based heterogeneous photo-Fenton catalyst in wastewater treatment: a review of recent advances, J. Environ. Chem. Eng. 10 (2022).
[2] Y. Xu, L. Xiao, J. Chen, Q. Wu, W. Yu, W. Zeng, Y. Shi, Y. Lu, Y. Liu, α-Fe_2O_3 based nanotherapeutics for near-infrared/dihydroartemisinin dual-augmented chemodynamic antibacterial therapy, Acta Biomater. 150 (2022) 367–379.
[3] A. Umar, A.A. Ibrahim, R. Kumar, H. Albargi, M.A. Alsaiari, F. Ahmed, Cubic shaped hematite (α-Fe_2O_3) micro-structures composed of stacked nanosheets for rapid ethanol sensor application, Sens Actuators B Chem. 326 (2021).
[4] J. Khan, S. Lin, J.C. Nizeyimana, Y. Wu, Q. Wang, X. Liu, Removal of copper ions from wastewater via adsorption on modified hematite (α-Fe_2O_3) iron oxide coated sand, J. Clean. Prod. 319 (2021).
[5] I. Dzyaloshinsky, A thermodynamic theory of "weak" ferromagnetism of antiferromagnetics, J. Phys. Chem. Solids 4 (4) (1958) 241–255.
[6] H. Shuwanto, H. Abdullah, D.-H. Kuo, Nanostructuring Bi-doped α-Fe_2O_3 thin-layer photoanode to advance the water oxidation performance, ACS Appl. Energy Mater. 5 (2022) 9902–9913.
[7] X. Wang, T. Wang, G. Si, Y. Li, S. Zhang, X. Deng, X. Xu, Oxygen vacancy defects engineering on Ce-doped α-Fe_2O_3 gas sensor for reducing gases, Sens Actuators B Chem. 302 (2020).
[8] S.I. Srikrishna Ramya, C.K. Mahadevan, Preparation and structural, optical, magnetic, and electrical characterization of Mn^{2+}/Co^{2+}/Cu^{2+} doped hematite nanocrystals, J. Solid State Chem. 211 (2014) 37–50.
[9] G. Neri, A. Bonavita, S. Ipsale, G. Rizzo, C. Baratto, G. Faglia, G. Sberveglieri, Pd- and Ca-doped iron oxide for ethanol vapor sensing, Mater. Sci. Eng. B Solid State Mater. Adv. Technol. 139 (2007) 41–47.
[10] P. Sun, C. Wang, X. Zhou, P. Cheng, K. Shimanoe, G. Lu, N. Yamazoe, Cu-doped α-Fe_2O_3 hierarchical microcubes: Synthesis and gas sensing properties, Sens. Actuators B Chem. 193 (2014) 616–622.
[11] M. Sorescu, L. Diamandescu, A. Tomescu, S. Krupa, Synthesis and sensing properties of zirconium-doped hematite nanoparticles, Phys. B Condens Matter 404 (2009) 2159–2165.
[12] C. Zhao, J. Bai, B. Huang, Y. Wang, J. Zhou, E. Xie, Grain refining effect of calcium dopants on gas-sensing properties of electrospun α-Fe2O3 nanotubes, Sens Actuators B Chem. 231 (2016) 552–560.
[13] S. Guo, H. Wang, W. Yang, H. Fida, L. You, K. Zhou, Scalable synthesis of Ca-doped α-Fe_2O_3 with abundant oxygen vacancies for enhanced degradation of organic pollutants through peroxymonosulfate activation, Appl. Catal. B 262 (2020).
[14] T. Zhang, J. Li, Z. Qin, C. Li, H. Gao, F. Zhao, H. Ma, Doping hematite with bismuth to enhance its catalytic and oxidizing properties, Chem. Eng. J. 421 (2021).
[15] R.N. Bhowmik, G. Vijayasri, R. Ranganathan, Structural characterization and ferromagnetic properties in Ga^{3+} doped α-Fe_2O_3 system prepared by coprecipitation route and vacuum annealing, J. Appl. Phys. 116 (2014).
[16] F.S. Freyria, G. Barrera, P. Tiberto, E. Belluso, D. Levy, G. Saracco, P. Allia, E. Garrone, B. Bonelli, Eu-doped α-Fe_2O_3 nanoparticles with modified magnetic properties, J. Solid State Chem. 201 (2013) 302–311.
[17] N. Popov, M. Ristić, M. Bošković, M. Perović, S. Musić, D. Stanković, S. Krehula, Influence of Sn doping on the structural, magnetic, optical and photocatalytic properties of hematite (α-Fe_2O_3) nanoparticles, J. Phys. Chem. Solids 161 (2022).
[18] V. Kumar, D.S. Ahlawat, S. AarifUl Islam, A. Singh, Ce doping induced modifications in structural, electrical and magnetic behaviour of hematite nanoparticles, Mater. Sci. Eng. B Solid State Mater. Adv. Technol. 272 (2021).
[19] N. Popov, M. Ristić, V. Kuncser, K. Zadro, N. Velinov, P. Badica, A. Alexandru-Dinu, N. Iacob, L. Kratofil Krehula, S. Musić, S. Krehula, Influence of erbium doping on the structural, magnetic and optical properties of hematite (α-Fe_2O_3) nanorods, J. Phys. Chem. Solids 169 (2022).
[20] P. Kumar, V. Sharma, J.P. Singh, A. Kumar, S. Chahal, K. Sachdev, K.H. Chae, A. Kumar, K. Asokan, D. Kanjilal, Investigations on magnetic and electrical properties of Zn doped Fe_2O_3 nanoparticles and their correlation with local electronic structures, J. Magn. Magn. Mater. 489 (2019).
[21] N. Popov, M. Bošković, M. Perović, K. Zadro, V. Gilja, L. Kratofil Krehula, M. Robić, M. Marciuš, M. Ristić, S. Musić, D. Stanković, S. Krehula, Effect of Ru^{3+} ions on the formation, structural, magnetic and optical properties of hematite (α-Fe_2O_3) nanorods, J. Magn. Magn. Mater. 538 (2021) 168316.
[22] S. Layek, K. Rout, M. Mohapatra, S. Anand, H.C. Verma, Structural and magnetic properties of dilute Ca^{2+} doped iron oxide nanoparticles, J. Nanosci. Nanotechnol. 16 (2016) 410–417.
[23] H. Wan, P. Rong, X. Liu, L. Yang, Y. Jiang, N. Zhang, R. Ma, S. Liang, H. Wang, G. Qiu, Morphological evolution and magnetic property of rare-earth-doped hematite nanoparticles: promising contrast agents for T1-weighted magnetic resonance imaging, Adv. Funct. Mater. 27 (2017).
[24] A. Samariya, S.N. Dolia, A.S. Prasad, P.K. Sharma, S.P. Pareek, M.S. Dhawan, S. Kumar, Size dependent structural and magnetic behaviour of CaFe2O4, Curr. Appl. Phys. 13 (5) (2013) 830–835.
[25] G. Lal, K. Punia, S.N. Dolia, P.A. Alvi, S. Dalela, S. Kumar, Rietveld refinement, Raman, optical, dielectric, Mössbauer and magnetic characterization of superparamagnetic fcc-CaFe2O4 nanoparticles, Ceram. Int. 45 (5) (2019) 5837–5847.
[26] M.C. Robert, M. Thavarani, N. Pavithra, S.B. Prasath, R. Saravanan, Y.B. Kannan, Influence of Zn2+ doping on CaFe2O4 spinel ferrites: an analysis of experimental charge density and magnetism, J. Supercond. Nov. Magn. 35 (5) (2022) 1281–1298.
[27] S. Okada, K. Takagi, K. Ozaki, Synthesis of submicron-sized acicular goethite and platelet-like hematite particles and dependence of magnetic properties of α-Fe particles on their shape and size, Mater. Chem. Phys. 171 (2016) 171–177.
[28] R.D. Shannon, C.T. Prewitt, Effective ionic radii in oxides and fluorides, Acta Crystallogr. Sect. B 25 (1969) 925–946.
[29] V.V. Korovushkin, A.V. Trukhanov, V.G. Kostishin, I.M. Isaev, S.V. Trukhanov, K. A. Astapovich, A.Y. Mironovich, Correlation between the chemical composition, crystal structure, and magnetic properties of hexagonal barium ferrite with Zn^{2+} heterovalent substitution, Inorg. Mater. 56 (2020) 707–715.
[30] Z. Šimša, Šimšová, J. Zemek, P.E. Wigen, M. Pardavi-Horvath, Search for Fe4+ in YIG: Ca garnet films, Le J. de Phys. Colloques 49 (1988) (C8-975-C8-976).
[31] L. Eiselt, R. Kruk, H. Hahn, A. Sarkar, Hole-doped high entropy ferrites: structure and charge compensation mechanisms in ($Gd_{0.2}$La0.2Nd0.2Sm0.2Y0.2) 1−xCaxFeO3, Int J. Appl. Ceram. Technol. (2022).
[32] D.B. Borgekov, A.L. Kozlovskiy, R.I. Shakirzyanov, A.T. Zhumazhanova, M. Zdorovets, D.I. Shlimas, Properties of perovskite-like lanthanum strontium

ferrite ceramics with variation in lanthanum concentration, Crystals 12 (2022) (1792).
[33] A.Y. Mironovich, V.G. Kostishin, R.I. Shakirzyanov, A.A. Mukabenov, S. A. Melnikov, A.I. Ril, H.I. Al-Khafaji, Effect of the Fe/Ba and Fe/Sr ratios on the phase composition, dielectric properties and magnetic characteristics of M-type hexaferrites prepared by the hydrothermal method, J. Solid State Chem. 316 (2022).
[34] E. Murad, Mössbauer spectroscopy of clays, soils and their mineral constituents, Clay Min. 45 (2010) 413–430.
[35] J. Jacob, M. Abdul Khadar, VSM and Mössbauer study of nanostructured hematite, J. Magn. Magn. Mater. 322 (2010) 614–621.
[36] J. André-Filho, L. León-Félix, J.A.H. Coaquira, V.K. Garg, A.C. Oliveira, Size dependence of the magnetic and hyperfine properties of nanostructured hematite (α-Fe_2O_3) powders prepared by the ball milling technique, Hyperfine Inter. 224 (2014) 189–196.
[37] S.J. Stewart, R.A. Borzi, E.D. Cabanillas, G. Punte, R.C. Mercader, Effects of milling-induced disorder on the lattice parameters and magnetic properties of hematite, J. Magn. Magn. Mater. 260 (2003) 447–545.
[38] E. Wolska, The structure of hydrohematite, Zeitsch. Kristallogr.-Cryst. Mater. 154 (1-4) (1981) 69–76.
[39] M.Z. Dang, D.G. Rancourt, J.E. Dutrizac, G. Lamarche, R. Provencher, Interplay of surface conditions, particle size, stoichiometry, cell parameters, and magnetism in synthetic hematite-like materials, Hyperfine Interact. 117 (1998) 271–319.
[40] E. Wolska, U. Schwertmann, Nonstoichiometric structures during dehydroxylation of goethite, Zeitsch. Kristallogr.-Cryst. Mater 189 (1-4) (1989) 223–238.
[41] S.A. Chen, P.J. Heaney, J.E. Post, T.B. Fischer, P.J. Eng, J.E. Stubbs, Superhydrous hematiteand goethite: A potential water reservoir in the red dust of Mars? Geology 49 (11) (2021) 1343–1347.
[42] E.C. Sklute, S. Kashyap, M.D. Dyar, J.F. Holden, T. Tague, P. Wang, S.J. Jaret, Spectral and morphological characteristics of synthetic nanophase iron (oxyhydr) oxides, Phys. Chem. Miner. 45 (1) (2018) 1–26.
[43] B.L.H.D. Weckler, H.D. Lutz, Lattice vibration spectra. Part XCV. Infrared spectroscopic studies on the iron oxide hydroxides goethite (α), akaganéite (β), lepidocrocite (γ), and feroxyhite (δ), Eur. J. Solid State Inorg. Chem. 35 (8-9) (1998) 531–544.
[44] E. Murad, Mossbauer spectroscopy of clays, soils and their mineral constituents, Clay Miner. 45 (4) (2010) 413–430.
[45] A.N. Christensen, T.R. Jensen, C.R.H. Bahl, E. DiMasi, Nano size crystals of goethite, α-FeOOH: synthesis and thermal transformation, J. Solid State Chem. 180 (2007) 1431–1435.